Journal of Hazardous Materials 344 (2018) 758–769

Contents lists available at ScienceDirect

Journal of Hazardous Materials

journal homepage: www.elsevier.com/locate/jhazmat

Research paper

Construction of plasmonic Ag modified phosphorous-doped ultrathin g-C_3N_4 nanosheets/$BiVO_4$ photocatalyst with enhanced visible-near-infrared response ability for ciprofloxacin degradation

Yaocheng Deng[a,b], Lin Tang[a,b,*], Chengyang Feng[a,b], Guangming Zeng[a,b,*], Jiajia Wang[a,b], Yaoyu Zhou[c], Yani Liu[a,b], Bo Peng[a,b], Haopeng Feng[a,b]

[a] College of Environmental Science and Engineering, Hunan University, Changsha, 410082, China
[b] Key Laboratory of Environmental Biology and Pollution Control, Hunan University, Ministry of Education, Changsha 410082, China
[c] College of Resources and Environment, Hunan Agricultural University, Changsha 410128, China

HIGHLIGHTS

- Novel Ag@PCNS/$BiVO_4$ nanocomposite was synthesized via an impregnated process combined with photoreduction method.
- Synergistic effects results in enhanced visible-near-infrared response ability.
- Boosted photocatalytic removal efficiency of ciprofloxacin.
- The effect of surface plasmonic resonance caused by metallic Ag contributed to the dual Z-scheme reaction mechanism.

GRAPHICAL ABSTRACT

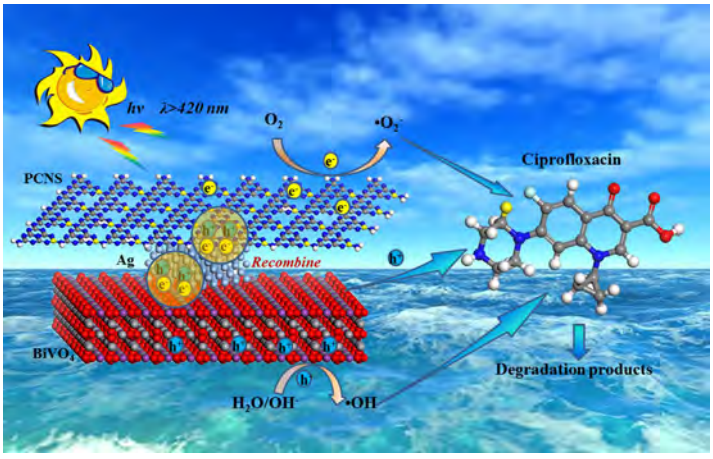

ARTICLE INFO

Article history:
Received 19 July 2017
Received in revised form 26 October 2017
Accepted 14 November 2017
Available online 15 November 2017

Keywords:
Photocatalysis
Dual Z-scheme
Ultrathin g-C_3N_4 nanosheets
Ciprofloxacin
Near-infrared response

ABSTRACT

To realize the full utilization of solar energy, the design of highly efficient photocatalyst with improved visible-near-infrared photocatalysis performance has attracted great attentions for environment pollutant removal. In this work, we rationally employed the surface plasmon resonance effect of metallic Ag in the phosphorus doped ultrathin g-C_3N_4 nanosheets (PCNS) and $BiVO_4$ composites to construct a ternary Ag@PCNS/$BiVO_4$ photocatalyst. It was applied for the photodegradation of ciprofloxacin (CIP), exhibiting 92.6% removal efficiency under visible light irradiation (λ > 420 nm) for 10 mg/L CIP, and presenting enhanced photocatalytic ability than that of single component or binary nanocomposites under near-infrared light irradiation (λ > 760 nm). The improved photocatalytic activity of the prepared Ag@PCNS/$BiVO_4$ nanocomposite can be attributed to the synergistic effect among the PCNS, $BiVO_4$ and Ag, which not only improves the visible light response ability and hinders the recombination efficiency of the photogenerated electrons and holes, but also retains the strong the redox ability of the photogenerated charges. According to the trapping experiment and ESR measurements results, •OH, h^+ and $•O_2^-$

* Corresponding authors at: College of Environmental Science and Engineering, Hunan University, Changsha, 410082, China
E-mail addresses: tanglin@hnu.edu.cn (L. Tang), zgming@hnu.edu.cn (G. Zeng).

https://doi.org/10.1016/j.jhazmat.2017.11.027

all participated in the photocatalytic degradation process. Considering the SPR effect of metallic Ag and the established local electric field around the interfaces, a dual Z-scheme electrons transfer mechanism was proposed.

1. Introduction

The abuse and discharge of pharmaceutical compounds in the environment cause great threat to human health. Ciprofloxacin (CIP), a second-generation fluoroquinolone (FQ) antibiotic, has been widely used to fight against variety diseases [1]. However, due to the proliferation effect of bacterial drug resistance even in trace concentration, CIP also brings about great harm to humans and eco-system. Now, CIP exists in different water resources, such as wastewater, surface water, ground water and even in drinking water [2–4]. The concentration of CIP in these environmental matrices mainly located at μg/L, in some freshwater ecosystems even reached mg/L. [5,6] Just the same as many other pharmaceutical chemicals, CIP cannot be removed efficiently by biodegradable process [7,8]. Thus the removal of CIP from the environment has already become an urgent issue, and highly efficient treatment method is needed.

Recently, the removal of environmental pollutants based on solar energy-driven semiconductor photocatalysis system has been developed rapidly [9–21]. Especially the efforts tend to broaden the light response ability of the semiconductors from visible to near-infrared light, because these two light account for most of the solar energy. However, seeking and designing satisfactory photocatalysts is still a huge challenge. Among various semiconductor photocatalysts, graphitic carbon nitride (g-C_3N_4) has attracted great attentions owing to its nontoxic, visible light response ability, proper energy band level and position and excellent physicochemical stability [22–24]. However, pristine g-C_3N_4 usually possesses limited visible light response ability. Therefore, the modification of g-C_3N_4 to enhance its visible light even near-infrared light response ability is necessary, and two main strategies can be applied. One is structure engineering and self-doping with other elements [23–27]. For example, the fabrication of phosphorous-doped ultrathin porous g-C_3N_4 presented enhanced photocatalytic hydrogen production ability and environment pollutants removal performance [28,29]. But owing to the intrinsic band-gap energy (~2.8 eV) of g-C_3N_4 and the fast recombination rate of the photogenerated electron and holes, the performance of modified g-C_3N_4 via this strategy still needs to be improved. The other strategy is to couple with another semiconductor to form heterojunction to accelerate the transformation of the photogenerated charges and acquire high light conversion efficiency [30–32].

Additionally, it is well known that the formation of heterojunction is beneficial to the electron transfer, such as *p-n* heterojunction, Schottky junction and Z-scheme electrons transfer mechanism. As for typical charge transfer mechanism (*p-n* junction or Schottky junction), the photogenerated charges is inevitable to experience the transfer process to reduce the recombination efficiency, resulting in the reduced redox ability [33]. Different from typical charge transfer mechanism, the Z-scheme mechanism possesses unique properties. It can retain the reductive electrons in the higher CB and oxidative holes in the lower VB, resulting in not only promoted separation rate but also strong redox ability of photogenerated charges [34–36]. So the combination of g-C_3N_4 with another semiconductor to construct Z-scheme would be an efficient strategy.

Another semiconductor material, bismuth vanadate ($BiVO_4$) also attracts great attention due to its relatively narrow band gap (2.4 eV), chemical stability and sufficient photocatalytic activity. And many researches have been focused on the use of $BiVO_4$ for the degradation of environmental contaminants. [37–39] Meanwhile, owing to the suitable bandgaps and band positions between g-C_3N_4 and $BiVO_4$, it is expected that formation of g-C_3N_4 and $BiVO_4$ hybrid composite could remarkably enhance the photocatalytic activity [40–46]. However, the studies on g-C_3N_4/$BiVO_4$ composite present different charge transfer pathways in different reaction system. Zhao et al. thought that the enhanced photocatalytic performance origins from the typical charge transfer process [45]. But Zhang and co-workers reported that due to the match bandgaps between g-C_3N_4 and $BiVO_4$, the photogenerated electrons on CB of $BiVO_4$ could rapidly recombine with photogenerated holes on VB of g-C_3N_4 to realize a novel Z-scheme system, resulting in the improved photocatalytic performance [46]. So, what are the reasons for the different results? The fact is that in a semiconductor heterojunction, these two different charge transfer process (typical charge transfer and Z-scheme mechanism) would co-exist, and in different reaction system, the prominent charge transfer mechanism would be different. Besides, the Z-scheme charge transfer usually competes with the typical charge transfer. In this regard, to speed up the desirable specific Z-scheme charge transfer process, an electron mediator is needed [31,33]. Among various materials, Ag usually plays the role of electron mediator in many photocatalytic systems [47–49]. However, due to the existence of the surface plasmon resonance-induced local electric field, Ag can also generate the electron-rich or hole-rich region under visible light irradiation, so the consideration of Ag just as an electron mediator is not accurate enough. Lately, Yu et al. proposed a dual Z-scheme concept to describe the electron transfer mechanism in the TiO_2-Ag-Cu_2O reaction system [50]. So we think it is possible to apply the SPR effect of Ag nanoparticles into the hybrid composite to design highly efficient photocatalysts with visible-near-infrared light response ability based on dual Z-scheme charge transfer mechanism.

Herein, we rationally applied the SPR effect of Ag into the phosphorous-doped ultrathin g-C_3N_4 nanosheets (PCNS) and $BiVO_4$ hybrid composites to design ternary Ag@PCNS/$BiVO_4$ photocatalyst. CIP was used as the target contaminant to evaluate the photocatalytic activity of the prepared samples. Under the optimum condition, the prepared Ag@PCNS/$BiVO_4$ composite presented 92.6% and 18.1% removal efficiencies under visible light and near infrared light irradiation within 120 min, respectively. Moreover, the reaction parameters for CIP removal have been systematically studied, such as the dosage of photocatalysts and the initial CIP concentration. Besides, the influences of cations and anions have been studied considering that real polluted water contains a variety of inorganic salts. The results show that the existence of CO_3^{2-} and PO_4^{3-} can significantly decrease photocatalytic activity of this reaction system, and others do not. This work provides a new insight into the understanding of SPR effect in the hybrid photocatalysts, and this strategy for the design of highly efficient dual Z-scheme photocatalysts could be expanded to other reaction system.

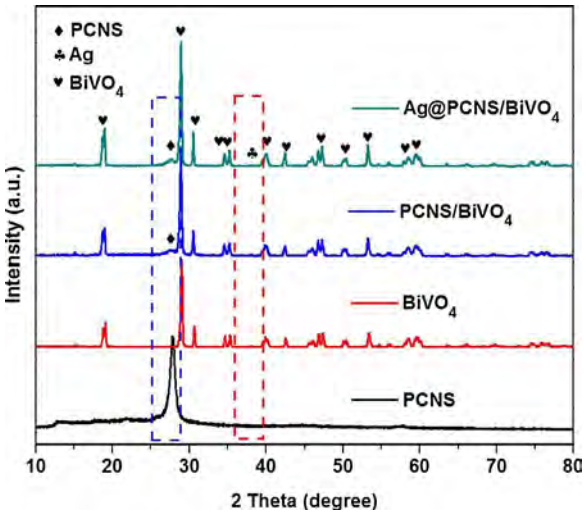

Fig 1. XRD patterns of the prepared PCNS, $BiVO_4$, PCNS/$BiVO_4$ and Ag@PCNS/$BiVO_4$ nanocomposites.

2. Experimental

This part can be seen in the supplement material.

3. Result and discussion

3.1. Structure and morphology characteristics

The crystalline phase of the samples was investigated by XRD analysis, and the results are disclosed in Fig. 1. For pure PCNS photocatalyst, only two diffraction peaks located on 27.3° and 13.4° are observed, representing the characteristic diffraction planes of (002) and (100), respectively (JCPDS 50-1250) [29]. As for pure $BiVO_4$, a series of diffraction peaks are consistent to the monoclinic phase of $BiVO_4$ (JCPDS 14-0688) [46]. For PCNS/$BiVO_4$ and Ag@PCNS/$BiVO_4$ samples, the co-existence of main peaks of the crystalline pattern of $BiVO_4$ and the weak characteristic peaks of PCNS means co-existence of PCNS and $BiVO_4$. It should be noted that no clear characteristic diffraction peaks of Ag can be observed in Ag@PCNS/$BiVO_4$ nanocomposite, which could be attributed to the relatively low amount of metallic Ag.

The SEM images are provided and presented in Fig. 2. From Fig. 2a, we can see that the prepared PCNS present nanosheets structure, which is in agreement with the reported literature [23,29]. While the prepared $BiVO_4$ presents blocked shape particles and smooth surface (Fig. 2b). As for ternary Ag@PCNS/$BiVO_4$ photocatalyst, the $BiVO_4$ nanoparticle were dispersed on the surface of PCNS, and the metallic Ag was also decorated on the surface of PCNS/$BiVO_4$ composites, which can be affirmed by the following analysis.

To obtain more detailed morphology, TEM and HR-TEM images were also provided (Fig. 3a and b). Fig. 3a discloses that the $BiVO_4$ nanoparticle and metallic Ag are uniformly dispersed on the surface of PCNS. And the result is also confirmed by the HR-TEM images of Ag@PCNS/$BiVO_4$ nanocomposite in Fig. 3b. The crystalline lattice of 0.237 nm belongs to Ag (111), and the crystalline lattice of 0.259 nm refers to the (200) plane of $BiVO_4$. Meanwhile, the amorphous part was corresponding to the PCNS nanosheets. The above mentioned results demonstrated the co-existence of Ag, $BiVO_4$ and PCNS, and their intimate connection with each other. Additionally, the EDS mapping clearly demonstrated the existence and uniform distribution of C, N, P, O, Bi, V and Ag elements, which gives strong evidence of the successful preparation of Ag@PCNS/$BiVO_4$ ternary nanocomposite.

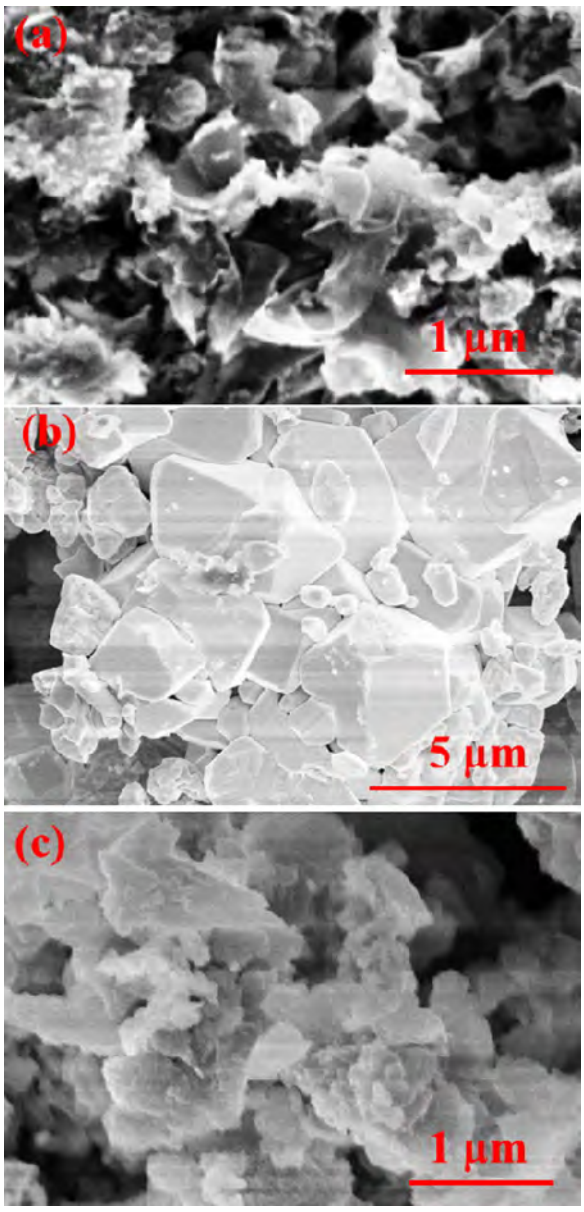

Fig. 2. (a) SEM images of PCNS, (b) $BiVO_4$ and (c) PCNS/$BiVO_4$ nanocomposites.

3.2. Surface chemical composition and group analysis

The FT-IR spectroscopy of the prepared samples is presented in Fig. 4. For pristine $BiVO_4$ photocatalyst, only one main peaks at 843 cm^{-1} are observed, which refer to the ν_1 symmetric stretching vibration of the VO_4 unit ν_1 (VO_4) [46]. As for PCNS, a series of peaks are obtained. The sharp peak at 807 cm^{-1} can be related to the *s*-triazine ring modes. Meanwhile, the peaks at 1568, 1423, 1320, and 1245 cm^{-1} are related to aromatic C—N stretching vibrations, while the peaks at 1643 cm^{-1} are attributed to C=N stretching vibration modes [29,51]. The FT-IR spectra of PCNS/$BiVO_4$ and Ag@PCNS/$BiVO_4$ heterojunctions are similar to those of the main peaks of pure PCNS and $BiVO_4$, suggesting that no obvious structural change of PCNS and $BiVO_4$ occurred during the preparation process of the photocatalyst.

To further investigate the composition of the as-prepared Ag@PCNS/$BiVO_4$ nanocomposite, XPS technique was utilized

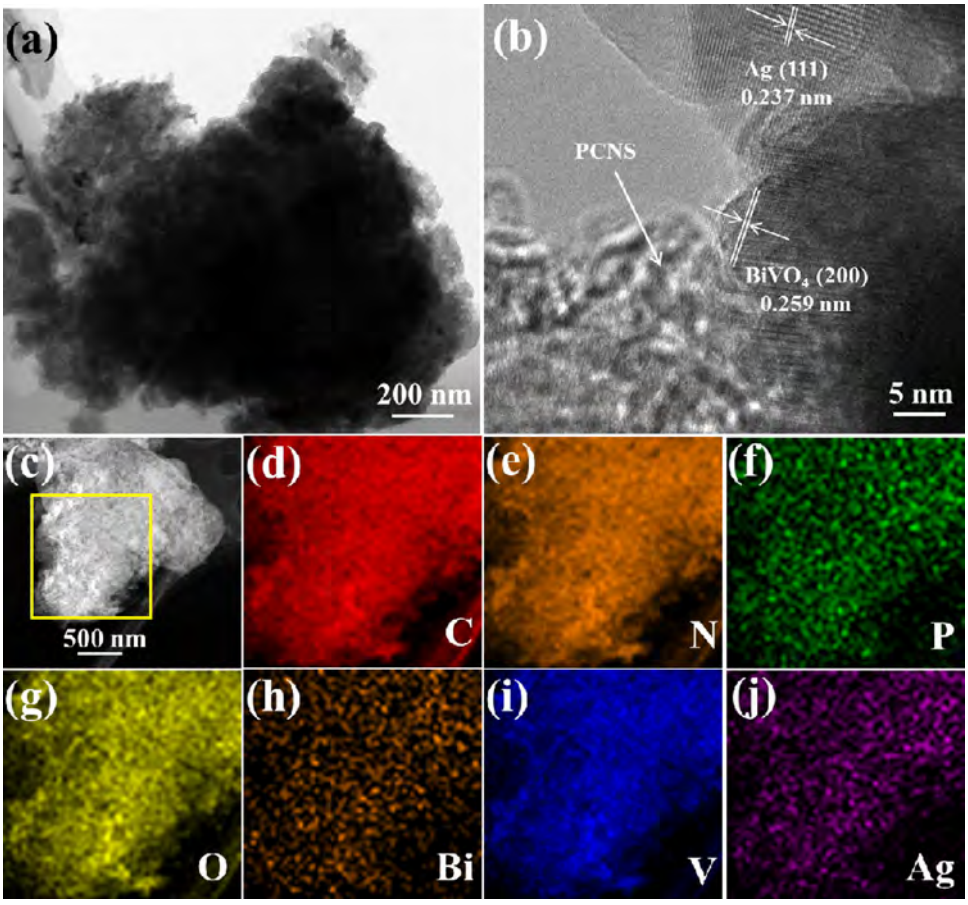

Fig. 3. (a) TEM image, (b) HR-TEM image of Ag@PCNS/$BiVO_4$ nanocomposite and the corresponding (c) HAADF-STEM image and (d–j) elements EDS mapping images.

(Fig. 5). The XPS survey spectrum is presented in Fig. 5a. It can be seen that the Bi, O, V, C, N and Ag elements could all be clearly observed, but the P element cannot be observed owing to the relatively low content in the composite. Fig. 5b shows the high-resolution XPS spectra of Bi 4f. The observed two main peaks at 163.8 eV and 168.4 eV belong to Bi $4f_{7/2}$ and Bi $4f_{5/2}$, respectively. As shown in Fig. 5c, the low peak at 523.8 eV belongs to V $2p_{1/2}$, and another main peak at 516.1 eV can be attributed to the V $2p_{3/2}$ [46]. In Fig. 5d, the spectra of O 1s can be separated to five peaks. The peak located at 529.4 eV belongs to the Bi—O bond of $(Bi_2O_2)^{2+}$ for $BiVO_4$. The peak at 530.9 eV can be attributed to the hydroxyl groups (O—H) on the surface. Further, due to the oxidation reaction happened in the preparation process, the characteristic peaks of C=O and C—O can be observed at 532.6 eV and 533.4 eV. Besides, a peak located at 531.9 eV could refer to $-NO_3^-$ owing to the acid treatment [40,52]. In Fig. 5e, the two peaks at 284.6 eV and 288.0 eV correspond to graphitic carbon (C—C) and sp^2-bounded carbon (C=N), respectively. Another weak peak at 286.1 eV could be the signal of the C—OH. As for the N 1s spectra in Fig. 5f, there are three main peaks located at 398.1 eV, 399.4 eV and 400.3 eV, corresponding to the C=N—C, N—$(C)_3$ and —NH_2 groups, respectively. Another minor peak at 403.7 eV can be attributed to the π-π* satellite [40]. The spectrum of P 2p only presented one main peak at 132.5 eV, which stands for P-N band (Fig. 5g) [29]. In the high-resolution XPS spectra of Ag 3d shown in Fig. 5h, the two main peaks observed at 368.1 eV and 374.1 eV can be assigned to metal Ag species [50]. The XPS results further demonstrated that the Ag@PCNS/$BiVO_4$ nanocomposite was successfully obtained.

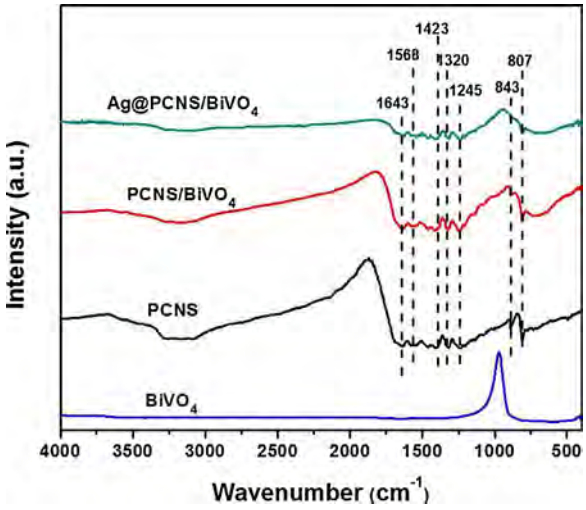

Fig. 4. The FT-IR spectra of the prepared samples.

3.3. Optical properties

To investigate the optical property of the prepared samples, the UV–vis DRS spectra are provided (Fig. 6). The pristine $BiVO_4$ shows an intense absorption band limited to 550 nm and PCNS presents absorption edge at around 480 nm. Interestingly, compared with $BiVO_4$, PCNS and PCNS/$BiVO_4$, Ag decorated PCNS/$BiVO_4$ photocatalyst exhibited an obviously enhanced visible light absorption edge

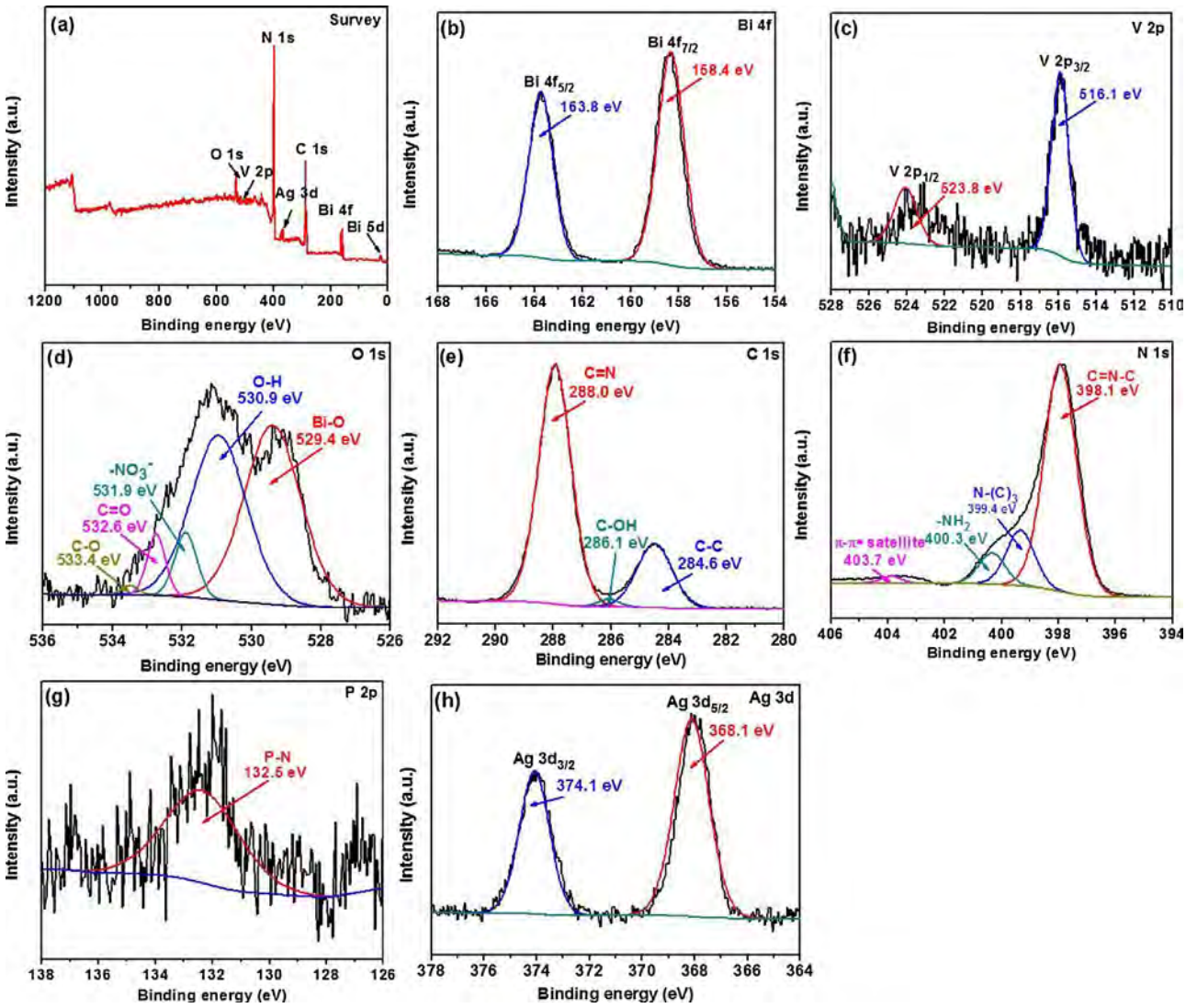

Fig. 5. The XPS spectra of Ag@PCNS/$BiVO_4$ nanocomposite.

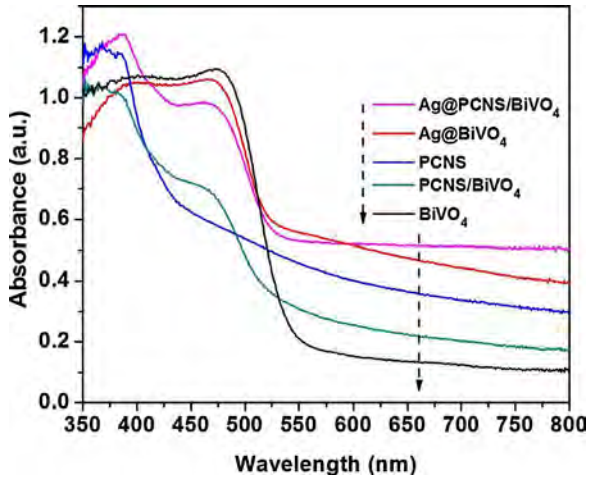

Fig. 6. UV–vis diffuse reflectance spectra of the prepared samples.

extending to 800 nm. The intense and broad absorption larger than 550 nm should origin from the strong surface plasmon resonance of Ag nanoparticles. Meanwhile, the $BiVO_4$ hybrid nanocomposite with Ag coated also presents enhanced absorption ability in the whole visible light region, which also confirmed the surface plasmon resonance effect of metallic Ag nanoparticles.

3.4. Photocatalytic performance of different photocatalysts

To evaluate the photocatalytic activities of the prepared samples, ciprofloxacin (CIP) was employed as a representative refractory pollutant, and the inherent pH value of 10 mg/L of CIP aqueous solution was 6.72. Meanwhile, we not only evaluated the prepared Ag@PCNS/$BiVO_4$ nanocomposite in visible light ($\lambda > 420$ nm), but also investigated its near infrared light irradiation response ability ($\lambda > 760$ nm). The relative results are presented in Fig. 7. Before exposed to the light irradiation, the reaction system was placed in dark condition with constant stirring for 30 min to establish the adsorption-desorption equilibrium. Besides, the photolysis experiments of CIP in both visible light and near infrared light irradiation were conducted, and the results indicated that the photolysis effect of CIP molecules can be ignored. Fig. 7a shows the concentration changes of CIP under visible light irradiation ($\lambda > 420$ nm). It can be seen that pristine $BiVO_4$ and PCNS Exhibits 61.6% and 74.8% of CIP decrease efficiency after 120 min, and PCNS/$BiVO_4$ and Ag@PCNS/$BiVO_4$ composites both present superior photocatalytic activities. Especially for the Ag@PCNS/$BiVO_4$ nanocomposite, the degradation efficiency of CIP

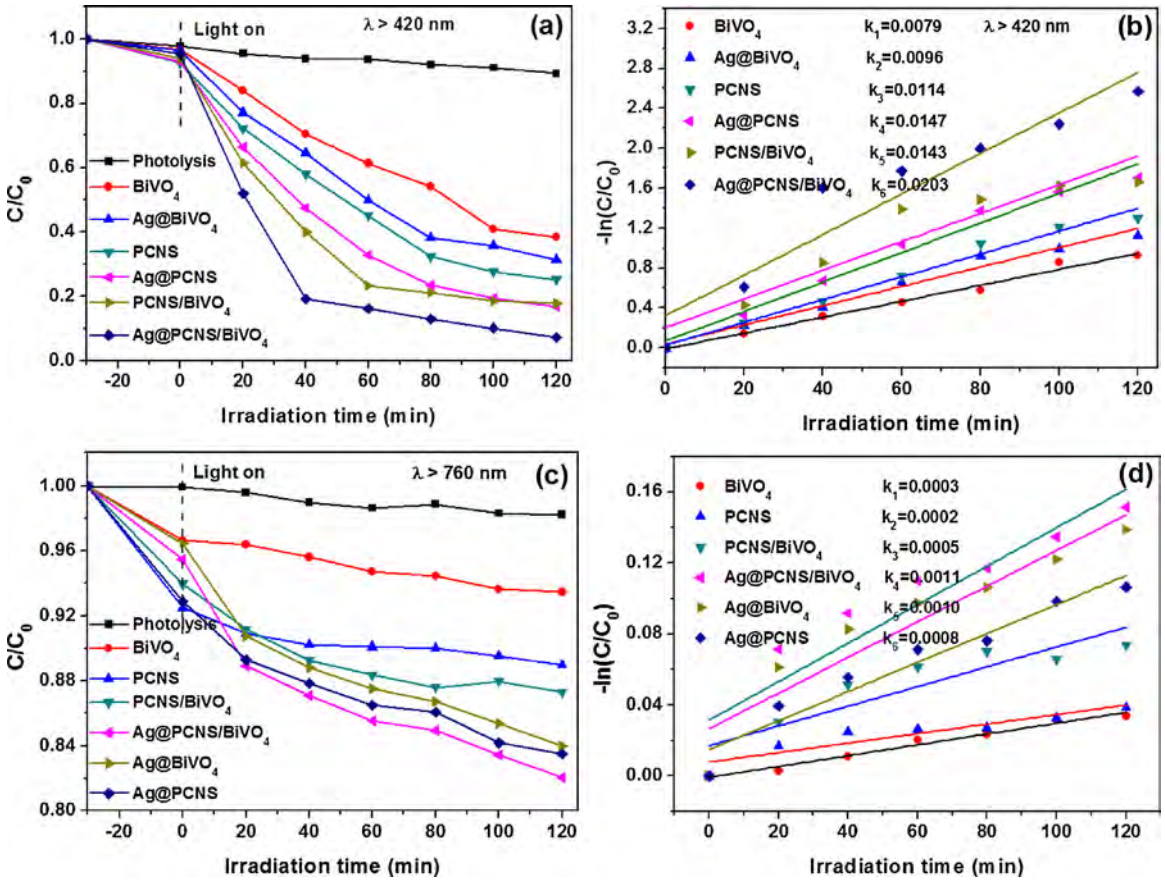

Fig. 7. Photodegradation of CIP with the existence of different samples and the variation in the normalized −ln (C/C0) of the CIP concentration as a function of irradiation time under different light irradiation: (a and b) visible light (λ > 420 nm) and (c and d) near-infrared light (λ > 760 nm).

reaches 92.6%, which is also higher than that of Ag@$BiVO_4$ (68.6%) and Ag@PCNS (82.2%). The enhanced photocatalytic performance of prepared Ag@PCNS/$BiVO_4$ nanocomposite can be attributed to the decoration of Ag nanoparticles in PCNS/$BiVO_4$ heterojunction photocatalysts via a photoreduction method. Since $BiVO_4$ was the electron-rich component in the PCNS/$BiVO_4$ composites, Ag nanoparticles can be deposited on $BiVO_4$ surfaces or on the interfaces between PCNS and $BiVO_4$, forming ohmic contact that could accelerate the charge transfer rate and enormously enhance the photocatalytic activity. Owing to the surface plasmon resonance properties, silver decorated on semiconductors can enhance the harvesting of visible light and the subsequent photocatalytic performance.

Further comparative studies of the concentration changes of CIP vs visible light irradiation time are shown in Fig. 7b. It is seen that there exists a linear relationship between the $-\ln(C/C_0)$ and reaction time, which indicated that the photodegradation of CIP followed a pseudo-first-order kinetic feature described as follows [53].

$$-\ln(C/C_0) = k_{app}t \quad (1)$$

where C is CIP concentration at time t, C_0 is the initial CIP concentration, and k_{app} is the first-order apparent rate constant. The photodegradation rate constants of CIP are experimentally determined to be 0.0079 for $BiVO_4$, 0.0098 for Ag@$BiVO_4$, 0.0114 for PCNS, 0.0147 for Ag@PCNS, 0.0143 for PCNS/$BiVO_4$ and 0.0203 for Ag@PCNS/$BiVO_4$ nanocomposite. Clearly, the prepared ternary Ag@PCNS/$BiVO_4$ nanocomposite led to remarkably enhanced photocatalytic activity toward CIP degradation in comparison to their individual counterpart or relative binary composites. The enhancement could be attributed to the excellent redox ability, promoted absorption of visible and spatial isolation of photogenerated carriers, which were achieved in the dual Z-scheme photocatalytic system. The mechanism will be explained in detail in mechanism section.

Considering that the near infrared light takes account of a great part of solar light, we also investigated the near infrared light response ability of Ag@PCNS/$BiVO_4$ nanocomposite [11]. As shown in Fig. 7c, the photocatalytic performance of all the photocatalysts remarkably declined under near infrared light irradiation (λ > 760 nm) due to the weak response ability of long wavelength light. However, owing to the existence of surface plasmon resonance effect of Ag nanoparticles, the prepared Ag@PCNS/$BiVO_4$ nanocomposite still presented much higher photocatalytic activity than pristine component or binary composites samples. The relative reaction kinetics is also provided in Fig. 7d. It can be seen that the prepared Ag@PCNS/$BiVO_4$ nanocomposite present higher reaction process than other samples. The results mentioned above demonstrated that Ag@PCNS/$BiVO_4$ nanocomposite showed superior photocatalytic performance under both visible light and near infrared light irradiation due to the synergistic effect among three semiconductors and stronger absorption in the light region, leading to the efficient photo-induced electron-hole pairs separation.

3.5. The effect of photocatalysts dosage and initial CIP concentration

Different dosages of Ag@PCNS/$BiVO_4$ were employed to study its effect on photodegradation efficiency. As shown in Fig. 8a, the photocatalytic degradation efficiencies increased from 53.4% to 92.6%

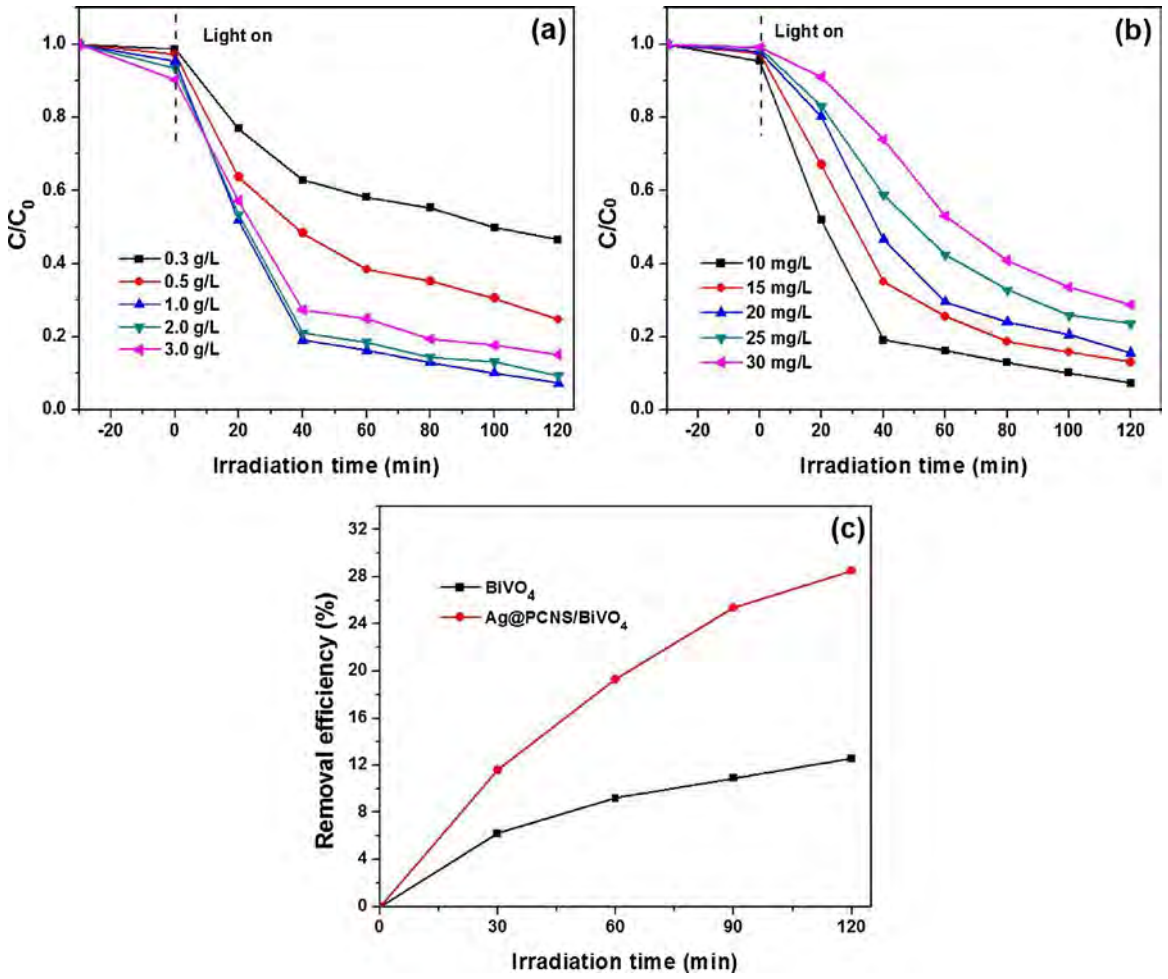

Fig. 8. The effects of (a) photocatalyst dosage with initial concentration of CIP as 10 mg/L and (b) initial CIP concentration with Ag@PCNS/$BiVO_4$ nanocomposite dosage as 1 g/L on photocatalysis performance of Ag@PCNS/$BiVO_4$ nanocomposite, and (c) total organic carbon (TOC) removal efficiency of the prepared $BiVO_4$ and Ag@PCNS/$BiVO_4$ nanocomposites.

Table 1
The parameters of the real water sample from Taozi Lake.

Sample	NH_3—N (mg L^{-1})	COD (mg L^{-1})	Cl^- (mg L^{-1})	NO_3^- (mg L^{-1})	TOC (mg L^{-1})	Fe (mg L^{-1})	Ca (mg L^{-1})	Mg (mg L^{-1})	Na (mg L^{-1})
Lake water	0.214	4.21	0.097	0.84	3.27	0.02	31.1	5.2	11.5

with the increase of the photocatalysts dosage from 0.3 to 1.0 g/L. The results showed that the optimal dosage is 1.0 g/L. Further increasing the photocatalyst dosage would bring about inhibitory effect. The results obtained can be explained by the following two reasons. Firstly, when the dosage of photocatalysts is in a relatively low content, the prepared Ag@PCNS/$BiVO_4$ nanocomposite cannot provide enough active sites for CIP molecules, which results in low photocatalytic removal efficiency. With the addition of photocatalyst dosage increases, more active sites will be available for CIP molecules, and then the degradation rate increases. Secondly, when the dosage of photocatalysts is excess and surpasses the optimal value, the turbidity of the reaction solution and the light-shielding effect of the photocatalysts will increase, so less light can reach the surface of Ag@PCNS/$BiVO_4$ nanocomposite, which reduces the generation of the photogenerated electrons and holes, and hinders the photocatalytic activity of the reaction system [54]. Therefore, the dosage of photocatalysts was set as 1.0 g/L in the following experiments.

Different initial concentrations of CIP pollutant also affect the photocatalytic activity of the photocatalysts. As shown in Fig. 8b, the degradation efficiency of 10 mg/L CIP solution is the highest among all. When the initial concentration of CIP increases from 10 mg/L to 30 mg/L, the photocatalytic removal efficiency of CIP decreases from 92.6% to 71.2%. Additionally, when the initial concentration of CIP increases, the kinetics process changes from the first order to near zeroth order. This transition in kinetics can be owing to the limited reactive oxygen species (ROS) and competitive effect of intermediate products. Similar phenomenon can also be found in other publication [53]. These results mean that higher initial pollutant concentration would inhibit the photocatalytic performance of the photocatalysts. When proper amount of CIP molecules are absorbed on the surface of Ag@PCNS/$BiVO_4$, they will serve as the consumer for the photogenerated electron-hole pairs and inhibit their recombination on the surface of the photocatalysts [54]. However, the consumer role of CIP molecules at higher initial concentration will disappear, replaced with its negative effect. Higher initial CIP solution concentration will decrease

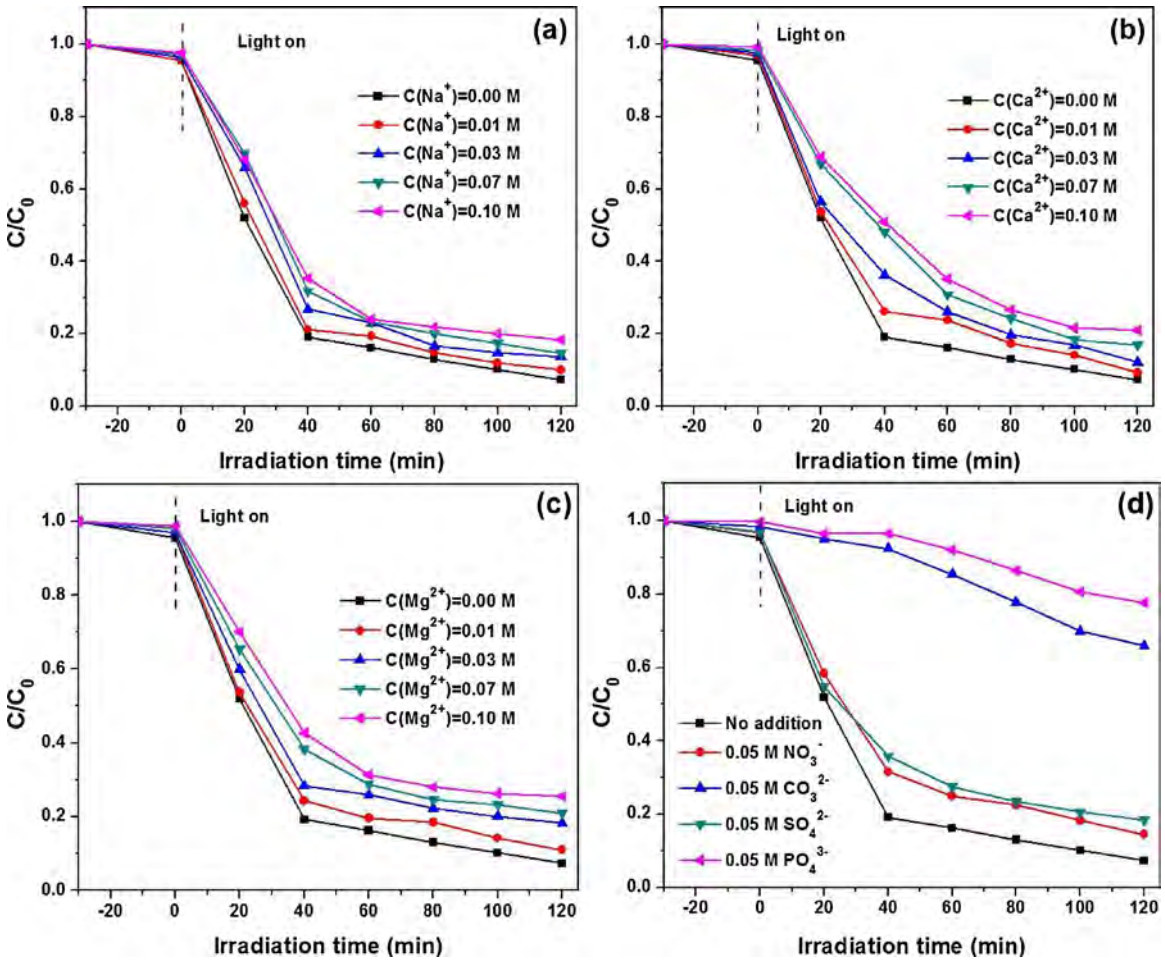

Fig. 9. Effect of the existence of different co-existence ions on the degradation of CIP over Ag@PCNS/$BiVO_4$ nanocomposite under visible light irradiation (λ > 420 nm): (a) cation, Na^+, (b) cation Ca^{2+}, (c) cation, Mg^{2+} and (d) anions, NO_3^-, CO_3^{2-}, SO_4^{2-} and PO_4^{3-}.

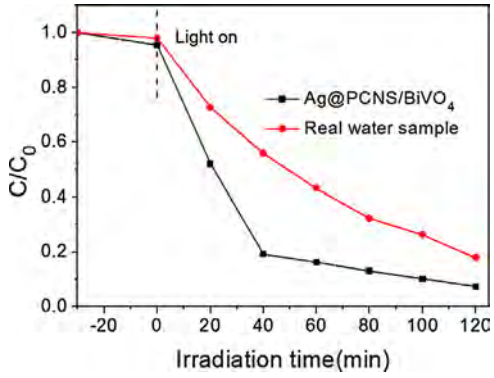

Fig. 10. Photocatalytic degradation of CIP in deionized water and real water under visible light irradiation.

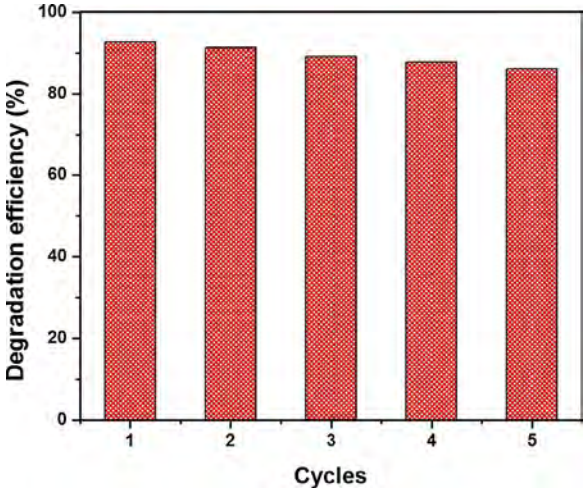

Fig. 11. Recycle experiments of Ag@PCNS/$BiVO_4$ nanocomposite for the photocatalytic degradation of CIP under visible light irradiation.

the transport opportunity of the photon and reduced penetration rate of the irradiation light in the reaction system, leading to limited photon utilized and excited by the photocatalysts. Meanwhile, higher CIP means the production of more intermediate products, which will compete with the CIP molecules for the limited reaction sites and result in the reduced reaction activity. Therefore, in the following experiments, 10 mg/L was used as the initial concentration of CIP.

The mineralization ability of the photocatalysts is vital to remove pollutants. As shown in Fig. 8c, the prepared Ag@PCNS/$BiVO_4$ obtained a total organic carbon (TOC) removal efficiency of 28.5% after 120 min, which was higher than that of pure $BiVO_4$ (12.6%) under similar conditions, indicating that the

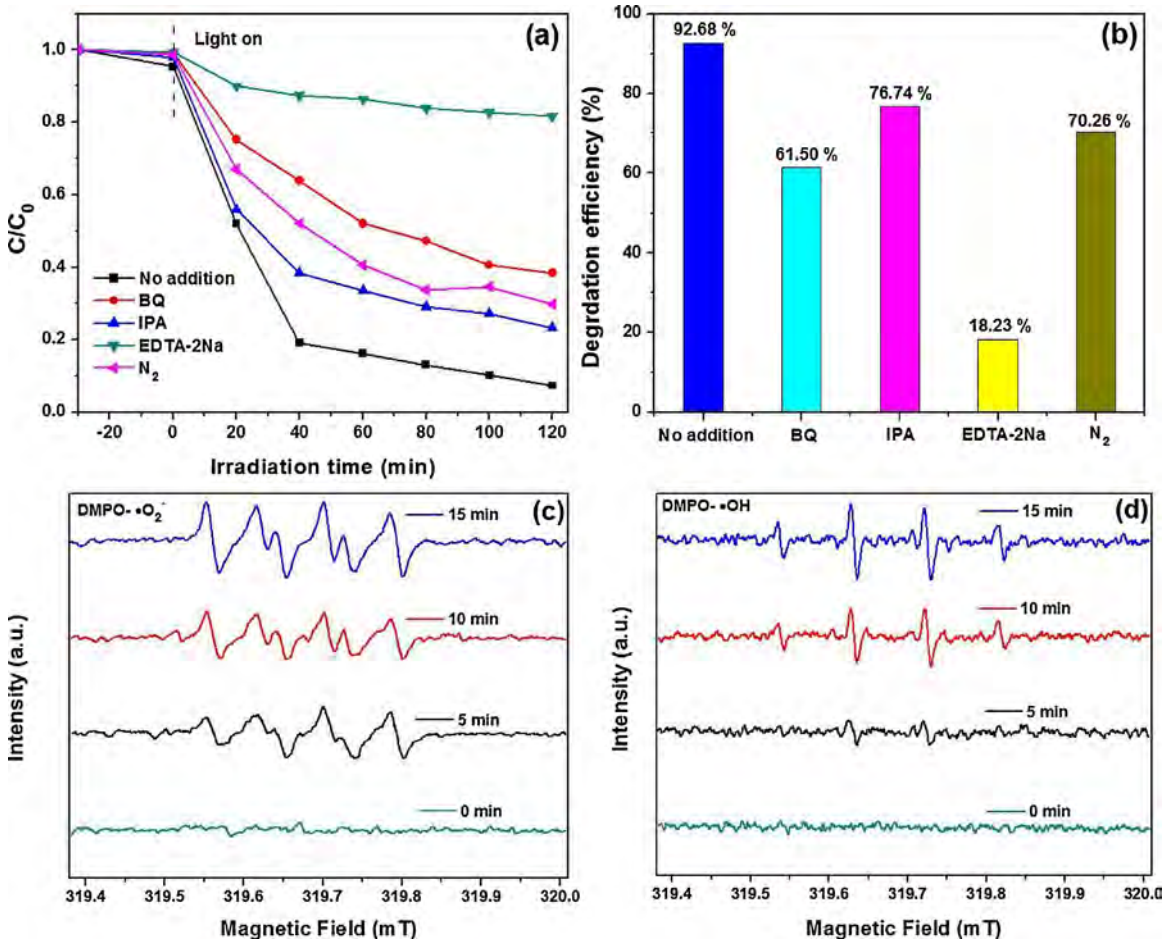

Fig. 12. (a and b) Active radical species trapping experiments for the photocatalytic degradation of CIP and the corresponding photocatalytic removal efficiency over Ag@PCNS/$BiVO_4$ nanocomposite under visible light irradiation, and (c and d) ESR spectra of radical adducts trapped by DMPO ($^{\bullet}O_2^-$ and $^{\bullet}OH$) in Ag@PCNS/$BiVO_4$ nanocomposite in the dark and with the visible light irradiation of 5 min, 10 min and 15 min.

prepared Ag@PCNS/$BiVO_4$ presents enhanced mineralization ability.

3.6. The influence of cations

It is well-known that different from deionized water, some inorganic salts are common in real waters, thus it is necessary to explore their effects on CIP removal process. For cations, we added NaCl, $CaCl_2$ or $MgCl_2$ to CIP solution, and the results could be seen in Fig. 9a–c. In Fig. 9a, we could find that Na^+ didn't have great influence on the photocatalytic performance. As for Ca^{2+} and Mg^{2+}, more inhibition effect has been presented, and both of these two ions performed similar results. When 0.01 M of these ions was added into the reaction system, the degradation process was inhibited at the beginning of irradiation process, and this effect decreased at 120 min. Besides, the increase of the ions concentrations showed similar effects, indicating that the increase of concentration just present slight hindering effect in the photocatalytic degradation process. The reason for the inhibition effect could be that the cations can bind to CIP to form metal complexes and be adsorbed on the surface of photocatalysts, slowing down the degradation process [55].

3.7. The influence of anion

As for anion ions, we added $NaNO_3$, Na_2SO_4, Na_2CO_3 or Na_3PO_4 to CIP solution, and the concentration of the ions was set as 0.05 M. As shown in Fig. 9d, the hindering effect of these anions (NO_3^-, SO_4^{2-}, CO_3^{2-} or PO_4^{3-}) was in the order as follows: $PO_4^{3-} > CO_3^{2-} > SO_4^{2-} > NO_3^-$. PO_4^{3-} presented the strongest inhibition effect and NO_3^- performed slight hindering effect. This phenomenon might be referring to the electrostatic repulsion effects. With the increase of the charge of these anions, the electrostatic repulsion effect increases, which will release the adsorption sites of CIP molecules and inhibit the adsorption process [56]. It should be noted that strong inhibition effect happened for CO_3^{2-}. Under these circumstances, both carbonate and bicarbonate ions existed in the reaction solution [57]. The existing carbonate and bicarbonate can serve as radical scavengers, which can consume the hydroxyl radicals produced at the surface of the Ag@PCNS/$BiVO_4$ photocatalyst, resulting in the decrease of the active radicals to react with the CIP molecules, and then the photocatalytic degradation of CIP was hindered greatly.

3.8. Real water sample treatment experiment

To simulate the real water sample close to the actual application condition, we used the lake water as the solvent to dissolve CIP as the reaction solution (10 mg/L) to investigate the photocatalytic activity of the prepared samples, and to analyze whether the prepared Ag@PCNS/$BiVO_4$ can maintain the high photocatalytic activity in real water sample. The lake water was collected from Taozi Lake in Changsha, China, and the parameters of the water sample from Taozi Lake are shown in Table 1. As shown in Fig. 10,

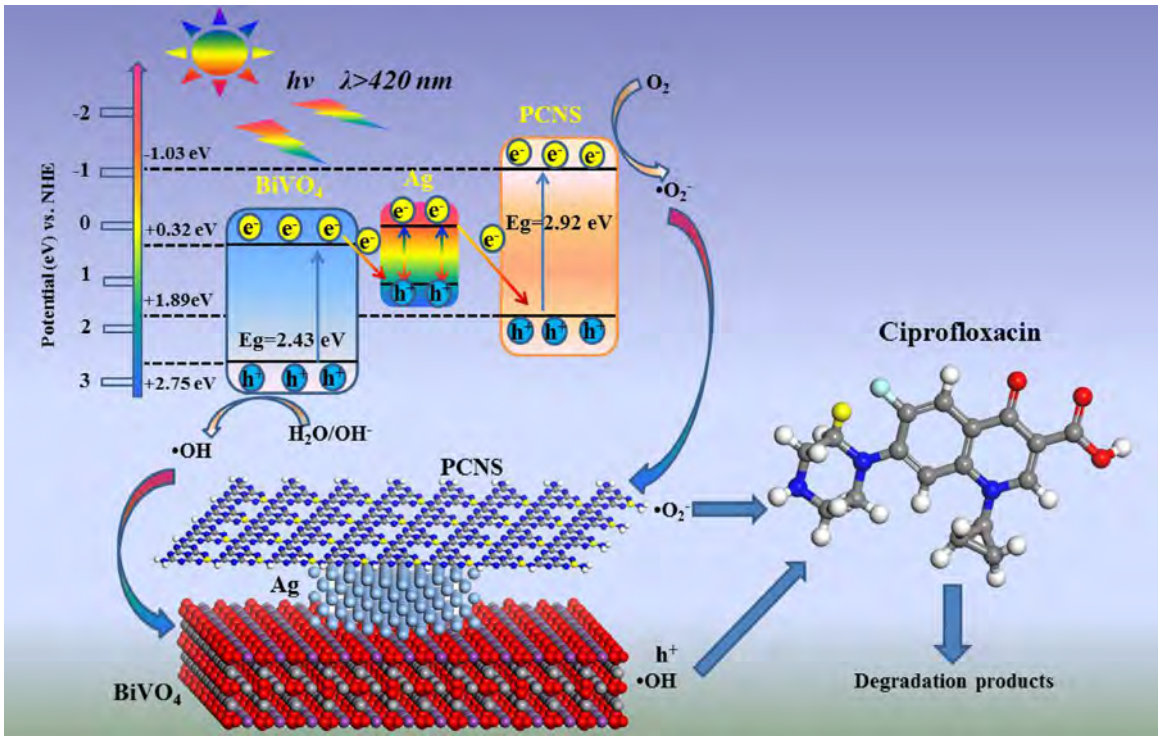

Fig. 13. Schematic illustration of the proposed photocatalytic reaction mechanism and photogenerated charges transfer pathway over Ag@PCNS/$BiVO_4$ nanocomposite towards CIP degradation under visible light irradiation (λ > 420 nm).

the results means that due to the existence of other competitive substances, the photocatalytic performance of the prepared samples was inhibited in some extent, but the eventual removal efficiency still reached nearly 80%, which indicated that the prepared sample has the potential for advanced treatment of real wastewater.

3.9. Photocatalyst recyclability

The reusability of the prepared Ag@PCNS/$BiVO_4$ was investigated to study the stability. The results of the first experiments and four repeated experiments are shown in Fig. 11. Even after four recovery processes, the degradation rate of CIP based on Ag@PCNS/$BiVO_4$ just experienced a slight decrease, the removal efficiency of CIP dropped from 92.6% to 86.1%, which indicates the high mechanical stability and performance of the photocatalyst.

3.10. Possible photocatalytic reaction mechanism

Generally, to verify the reaction process and electron transfer mechanism, the roles of three common active oxidant species, hydroxyl radical (•OH), hole (h^+) and superoxide radical ($•O_2^-$), need to be investigated. Herein, isopropanol (IPA), ethylenediamintetraacetic acid disodium (EDTA-2Na) and 1,4-benzoquinone (BQ) were used as the scavengers for •OH, h^+ and $•O_2^-$, respectively [13,47,58]. The addition dosage of these scavengers was 1 mM, and the results are presented in Fig. 12a and b. It can be seen that the photodegradation process of CIP have been inhibited in some extent with the addition of IPA, indicating that the •OH species participated in CIP removal process. However, when EDTA-2Na was added, the photocatalytic degradation efficiency of CIP sharply decreased from 92.68% to 18.23%, indicating that the h^+ species was the major reaction species. Meanwhile, the photocatalytic removal efficiency of CIP was hindered greatly with the addition of BQ, implying that $•O_2^-$ radical species also played vital role in the photocatalytic degradation process. Moreover, the experiment of purging of N_2 without the addition of any scavenges was carried out to confirm the function of $•O_2^-$ species. Similarly, the greatly decreased CIP degradation efficiency happened. Based on the results obtained in the scavengers experiment, it is clear to conclude that h^+ and $•O_2^-$ play the major role for the CIP degradation in the reaction system, and the role of •OH cannot be ignored either.

To further definitely affirm the generation of $•O_2^-$ and •OH species, the ESR spin-trap measurement based on Ag@PCNS/$BiVO_4$ photocatalyst under visible light irradiation was conducted [59]. All the experiments were operated under dark condition and visible light irradiation of 5 min, 10 min and 15 min. As shown in Fig. 12c, some characteristic peaks of DMPO-$•O_2^-$ are observed for Ag@PCNS/$BiVO_4$ nanocomposite under visible light irradiation and the signal intensities gradually increase with the increase of time. However, no any signals were detected in dark. Similarly, DMPO-•OH adducts are also detected successfully in aqueous dispersion of this composite, where four characteristic peaks of the DMPO-•OH are observed just with 5 mins irradiation (Fig. 12d). The ESR results suggest that $•O_2^-$ and •OH radical species could be generated by Ag@PCNS/$BiVO_4$ composite under visible light irradiation, which is consistent with radical-trapping photocatalytic experimental results.

Therefore, based on the above experimental results and analysis, a dual Z-scheme photocatalytic mechanism of the prepared Ag@PCNS/$BiVO_4$ nanocomposite is proposed and illustrated in Fig. 13. According to previous study, the CB of $BiVO_4$ and PCNS are 2.43 eV and 1.89 eV, respectively. The VB of $BiVO_4$ and PCNS are 0.32 eV and −1.03 eV, respectively [29,46]. During the preparation process of Ag@PCNS/$BiVO_4$ composite, the Fermi levels among the interface of PCNS, Ag and $BiVO_4$ have reached equilibrium. Then in the photodegradation process, when the reaction system is exposed to the visible light irradiation, both PCNS and $BiVO_4$ can be excited to generate photoexcited electron-hole pairs. Due to the existence

of metallic Ag, the electrons generated on the CB of $BiVO_4$ will transfer to metallic Ag. Meanwhile, owing to the strong SPR effect, the surface of metallic Ag will establish an enhanced local electric field, leading to the photogenerated electrons of Ag transport to VB of PCNS and recombine with the holes via plasmon-induced resonance energy transfer or direct electron migration. Subsequently, the remained photogenerated electrons in the CB of PCNS own the ability to react with dissolved O_2 to generate $^{\bullet}O_2^-$, and meanwhile, the holes accumulated on the VB of $BiVO_4$ possess enough energy to react with OH^- or H_2O to generate $^{\bullet}OH$ or react with CIP molecules directly. This dual Z-scheme charge transfer mechanism can bring about both promoted electrons and holes transfer, and high redox ability of the photogenerated charge without extra transmission. Due to the fact that this charge transfer pathway can be regarded to the combination of two Z-scheme processes, the "dual Z-scheme" reaction mechanism was proposed so as to describe the reaction process more accurately.

4. Conclusion

In summary, we rationally applied the SPR effect of metallic Ag into the PCNS/$BiVO_4$ nanocomposite to construct a ternary dual Z-scheme reaction system based on Ag@PCNS/$BiVO_4$. The prepared Ag@PCNS/$BiVO_4$ composite perform improved photodegradation rate for the CIP removal, presenting 92.6% removal efficiency under visible light irradiation within 120 min, and also presents enhanced photocatalytic activity under near infrared light irradiation. Besides, it presents mineralization ability with 28.5% TOC removal efficiency of CIP. The remarkable photodegradation performance of prepared Ag@PCNS/$BiVO_4$ for CIP removal can be contributed to the following two reasons: 1) The synergetic effect among the Ag, PANS and $BiVO_4$ in ternary Ag@PCNS/$BiVO_4$ composite can enhance the visible light utilization ability; 2) The strong SPR effect caused by Ag nanoparticles lead to the establishment of the local electric field, which contributed to the dual Z-scheme charge transfer pathway in the reaction process. This dual Z-scheme charge transfer mechanism can bring about both fast transportation of the photogenerated electron-hole pairs and strong redox ability, which results in the remarkable photocatalytic performance of the prepared Ag@PCNS/$BiVO_4$. This study provides a new insight into the designing of highly efficient photocatalyst based on metallic Ag, and help for the in-depth understanding of the dual Z-scheme charge transfer mechanism with surface plasmon resonance effect.

Acknowledgments

The study was financially supported by Projects 51579096, 51222805, 51521006, 51508175 and 51409024 supported by National Natural Science Foundation of China, the National Program for Support of Top-Notch Young Professionals of China (2012), the Program for New Century Excellent Talents in University from the Ministry of Education of China (NCET-11-0129), the Hunan Province Innovation Foundation for Postgraduate (CX2015B095).

Appendix A. Supplementary data

Supplementary data associated with this article can be found, in the online version, at https://doi.org/10.1016/j.jhazmat.2017.11.027.

References

[1] X. Zhang, R. Li, M. Jia, S. Wang, Y. Huang, C. Chen, Degradation of ciprofloxacin in aqueous bismuth oxybromide (BiOBr) suspensions under visible light irradiation: a direct hole oxidation pathway, Chem. Eng. J. 274 (2015) 290–297.
[2] M.J. Benotti, R.A. Trenholm, J.C. Vanderford, B.D. Stanford, S.A. Snyder, Pharmaceuticals and endocrine disrupting compounds in U.S. drinking water, Environ. Sci. Technol. 43 (2009) 597–603.
[3] X. Hu, Q. Zhou, Y. Luo, Occurrence and source analysis of typical veterinary antibiotics in manure soil, vegetables and groundwater from organic vegetable bases, northern China, Environ. Pollut. 158 (2010) 2992–2998.
[4] I. Michael, L. Rizzo, C.S. McArdell, C.M. Manaia, C. Merlin, T. Schwartz, C. Dagot, D. Fatta-Kassinos, Urban wastewater treatment plants as hotspots for the release of antibiotics in the environment: a review, Water Res. 47 (2013) 957–995.
[5] B. Petrie, R. Barden, B. Kasprzyk-Hordern, A review on emerging contaminants in wastewaters and the environment: current knowledge, understudied areas and recommendations for future monitoring, Water Res. 72 (2015) 3–27.
[6] S.R. Hughes, P. Kay, L.E. Brown, Global synthesis and critical evaluation of pharmaceutical data sets collected from river systems, Environ. Sci. Technol. 47 (2013) 661–677.
[7] M.D. Adjei, T.M. Heinze, J. Deck, J.P. Freeman, A.J. Williams, J.B. Sutherland, Transformation of the antibacterial agent norfloxacin by environmental mycobacteria, Appl. Environ. Microbiol. 72 (2006) 5790–5793.
[8] L. Tang, G.M. Zeng, G.L. Shen, Y.P. Li, Y. Zhang, D.L. Huang, Rapid detection of picloram in agricultural field samples using a disposable immunomembrane-based electrochemical sensor, Environ. Sci. Technol. 42 (2008) 1207–1212.
[9] X. Zhang, P. Zhang, L. Wang, H. Gao, J. Zhao, C. Liang, J. Hu, G. Shao, Template-oriented synthesis of monodispersed SnS_2@SnO_2 hetero-nanoflowers for Cr(VI) photoreduction, Appl. Catal. B-Environ. 192 (2016) 17–25.
[10] W. Wang, X. Huang, S. Wu, Y. Zhou, L. Wang, H. Shi, Y. Liang, B. Zou, Preparation of p–n junction Cu_2O/$BiVO_4$ heterogeneous nanostructures with enhanced visible-light photocatalytic activity, Appl. Catal. B-Environ. 134–135 (2013) 293–301.
[11] Y. Zhu, Y. Wang, Q. Ling, Y. Zhu, Enhancement of full-spectrum photocatalytic activity over $BiPO_4$/Bi_2WO_6 composites, Appl. Catal. B-Environ. 200 (2017) 222–229.
[12] Y.C. Deng, L. Tang, G.M. Zeng, H.R. Dong, M. Yan, J.J. Wang, W. Hu, J.J. Wang, Y.Y. Zhou, J. Tang, Enhanced visible light photocatalytic performance of polyaniline modified mesoporous single crystal TiO_2 microsphere, Appl. Surf. Sci. 387 (2016) 882–893.
[13] Y.C. Deng, L. Tang, G.M. Zeng, J.J. Wang, Y.Y. Zhou, J.J. Wang, J. Tang, Y.N. Liu, B. Peng, F. Chen, Facile fabrication of a direct Z-scheme Ag_2CrO_4/g-C_3N_4 photocatalyst with enhanced visible light photocatalytic activity, J. Mol. Catal. A-Chem. 421 (2016) 209–221.
[14] F. Chen, Q. Yang, X. Li, G. Zeng, D. Wang, C. Niu, J. Zhao, H. An, T. Xie, Y. Deng, Hierarchical assembly of graphene-bridged Ag_3PO_4/Ag/$BiVO_4$ (040) Z-scheme photocatalyst: an efficient, sustainable and heterogeneous catalyst with enhanced visible-light photoactivity towards tetracycline degradation under visible light irradiation, Appl. Catal. B-Environ. 200 (2017) 330–342.
[13] Y.C. Deng, L. Tang, G.M. Zeng, J.J. Wang, Y.Y. Zhou, J.J. Wang, J. Tang, Y.N. Liu, B. Peng, F. Chen, Facile fabrication of a direct Z-scheme Ag_2CrO_4/g-C_3N_4 photocatalyst with enhanced visible light photocatalytic activity, J. Mol. Catal. A-Chem. 421 (2016) 209–221.
[14] F. Chen, Q. Yang, X. Li, G. Zeng, D. Wang, C. Niu, J. Zhao, H. An, T. Xie, Y. Deng, Hierarchical assembly of graphene-bridged Ag_3PO_4/Ag/$BiVO_4$ (040) Z-scheme photocatalyst: an efficient, sustainable and heterogeneous catalyst with enhanced visible-light photoactivity towards tetracycline degradation under visible light irradiation, Appl. Catal. B-Environ. 200 (2017) 330–342.
[15] P. Singh, B. Priya, P. Shandilya, P. Raizada, N. Singh, B. Pare, S.B. Jonnalagadda, Photocatalytic mineralization of antibiotics using 60% WO_3/BiOCl stacked to graphene sand composite and chitosan, Arab. J. Chem. (2016).
[16] B. Priya, P. Raizada, N. Singh, P. Thakur, P. Singh, Adsorptional photocatalytic mineralization of oxytetracycline and ampicillin antibiotics using Bi_2O_3/BiOCl supported on graphene sand composite and chitosan, J. Colloid Interface Sci. 479 (2016) 271–283.
[17] B. Priya, P. Shandilya, P. Raizada, P. Thakur, N. Singh, P. Singh, Photocatalytic mineralization and degradation kinetics of ampicillin and oxytetracycline antibiotics using graphene sand composite and chitosan supported BiOCl, J. Mol. Catal. A Chem. 423 (2016) 400–413.
[18] S. Gautam, P. Shandilya, V.P. Singh, P. Raizada, P. Singh, Solar photocatalytic mineralization of antibiotics using magnetically separable $NiFe_2O_4$ supported onto graphene sand composite and bentonite, J. Water Process Eng. 14 (2016) 86–100.
[19] S. Gautam, P. Shandilya, B. Priya, V.P. Singh, P. Raizada, R. Rai, M.A. Valente, P. Singh, Superparamagnetic $MnFe_2O_4$ dispersed over graphitic carbon sand composite and bentonite as magnetically recoverable photocatalyst for antibiotic mineralization, Sep. Purif. Technol. 172 (2017) 498–511.
[20] Y. Deng, L. Tang, G. Zeng, C. Feng, H. Dong, J. Wang, H. Feng, Y. Liu, Y. Zhou, Y. Pang, Plasmonic resonance excited dual Z-scheme $BiVO_4$/Ag/Cu_2O nanocomposite: synthesis and mechanism for enhanced photocatalytic performance in recalcitrant antibiotic degradation, Environ. Sci.: Nano 4 (2017) 1494–1511.
[21] Y.C. Deng, L. Tang, G.M. Zeng, J.J. Wang, Y.Y. Zhou, J.J. Wang, J. Tang, L.L. Wang, C.Y. Feng, Facile fabrication of mediator-free Z-scheme photocatalyst of phosphorous-doped ultrathin graphitic carbon nitride nanosheets and bismuth vanadate composites with enhanced tetracycline degradation under visible light, J. Colloid Interf. Sci. 509 (2018) 219–234.

[22] S. Yang, Y. Gong, J. Zhang, L. Zhan, L. Ma, Z. Fang, R. Vajtai, X. Wang, P.M. Ajayan, Exfoliated graphitic carbon nitride nanosheets as efficient catalysts for hydrogen evolution under visible light, Adv. Mater. 25 (2013) 2452–2456.
[23] P. Niu, L. Zhang, G. Liu, H.-M. Cheng, Graphene-like carbon nitride nanosheets for improved photocatalytic activities, Adv. Funct. Mater. 22 (2012) 4763–4770.
[24] Y. Zhou, L. Zhang, W. Huang, Q. Kong, X. Fan, M. Wang, J. Shi, N-doped graphitic carbon-incorporated g-C_3N_4 for remarkably enhanced photocatalytic H_2 evolution under visible light, Carbon 99 (2016) 111–117.
[25] Z. Lin, X. Wang, Nanostructure engineering and doping of conjugated carbon nitride semiconductors for hydrogen photosynthesis, Angew. Chem. Int. Ed. 52 (2013) 1735–1738.
[26] Q. Lin, L. Li, S. Liang, M. Liu, J. Bi, L. Wu, Efficient synthesis of monolayer carbon nitride 2D nanosheet with tunable concentration and enhanced visible-light photocatalytic activities, Appl. Catal. B-Environ. 163 (2015) 135–142.
[27] M. Zhang, W. Jiang, D. Liu, J. Wang, Y. Liu, Y. Zhu, Y. Zhu, Photodegradation of phenol via C_3N_4-agar hybrid hydrogel 3D photocatalysts with free separation, Appl. Catal. B-Environ. 183 (2016) 263–268.
[28] Y.C. Deng, L. Tang, G.M. Zeng, Z.J. Zhu, M. Yan, Y.Y. Zhou, J.J. Wang, Y.N. Liu, J.J. Wang, Insight into highly efficient simultaneous photocatalytic removal of Cr(VI) and 2,4-diclorophenol under visible light irradiation by phosphorus doped porous ultrathin g-C_3N_4 nanosheets from aqueous media: performance and reaction mechanism, Appl. Catal. B: Environ. 203 (2017) 343–354.
[29] J. Ran, T.Y. Ma, G. Gao, X.-W. Du, S.Z. Qiao, Porous P-doped graphitic carbon nitride nanosheets for synergistically enhanced visible-light photocatalytic H_2 production, Energy Environ. Sci. 8 (2015) 3708–3717.
[30] J.J. Wang, L. Tang, G.M. Zeng, Y.C. Deng, Y.N. Liu, L.L. Wang, Y.Y. Zhou, Z. Guo, J.J. Wang, C. Zhang, Atomic scale g-C_3N_4/Bi_2WO_6 2D/2D heterojunction with enhanced photocatalytic degradation of ibuprofen under visible light irradiation, Appl. Catal. B: Environ. 209 (2017) 285–294.
[31] J.J. Wang, L. Tang, G.M. Zeng, Y.N. Liu, Y.Y. Zhou, Y.C. Deng, J.J. Wang, B. Peng, Plasmonic bi metal deposition and g-C_3N_4 coating on Bi_2WO_6 microspheres for efficient visible light photocatalysis, ACS Sustain. Chem. Eng. 5 (2017) 1062–1072.
[32] H. Wang, X. Yuan, Y. Wu, G. Zeng, X. Chen, L. Leng, H. Li, Synthesis and applications of novel graphitic carbon nitride/metal-organic frameworks mesoporous photocatalyst for dyes removal, Appl. Catal. B-Environ. 174-175 (2015) 445–454.
[33] P. Zhou, J. Yu, M. Jaroniec, All-solid-state Z-scheme photocatalytic systems, Adv. Mater. 26 (2014) 4920–4935.
[34] K. Maeda, D. Lu, K. Domen, Solar-driven Z-scheme water splitting using modified $BaZrO_3$-$BaTaO_2N$ solid solutions as photocatalysts, ACS Catal. 3 (2013) 1026–1033.
[35] Y. Hong, Y. Jiang, C. Li, W. Fan, X. Yan, M. Yan, W. Shi, In-situ synthesis of direct solid-state Z-scheme V_2O_5/g-C_3N_4 heterojunctions with enhanced visible light efficiency in photocatalytic degradation of pollutants, Appl. Catal. B-Environ. 180 (2016) 663–673.
[36] D. Xu, B. Cheng, S. Cao, J. Yu, Enhanced photocatalytic activity and stability of Z-scheme Ag_2CrO_4-GO composite photocatalysts for organic pollutant degradation, Appl. Catal. B-Environ. 164 (2015) 380–388.
[37] D.K. Ma, M.L. Guan, S.S. Liu, Y.Q. Zhang, C.W. Zhang, Y.X. He, S.M. Huang, Controlled synthesis of olive-shaped Bi_2S_3/$BiVO_4$ microspheres through a limited chemical conversion route and enhanced visible-light-responding photocatalytic activity, Dalton Trans. 41 (2012) 5581–5586.
[38] Y. Liu, Y. Zhang, H. Guo, X. Cheng, H. Liu, W. Tang, Persulfate-assisted photodegradation of diethylstilbestrol using monoclinic $BiVO_4$ under visible-light irradiation, Environ. Sci. Pollut. Res. 24 (2017) 3739–3747.
[39] M.J. Nalbandian, M. Zhang, J. Sanchez, Y.-H. Choa, D.M. Cwiertny, N.V. Myung, Synthesis and optimization of $BiVO_4$ and co-catalyzed $BiVO_4$ nanofibers for visible light-activated photocatalytic degradation of aquatic micropollutants, J. Mol. Catal. A-Chem. 404-405 (2015) 18–26.
[40] H.J. Kong, D.H. Won, J. Kim, S.I. Woo, Sulfur-doped g-C_3N_4/$BiVO_4$ composite photocatalyst for water oxidation under visible light, Chem. Mater. 28 (2016) 1318–1324.
[41] Y. Ji, J. Cao, L. Jiang, Y. Zhang, Z. Yi, G–C_3N_4/$BiVO_4$ composites with enhanced and stable visible light photocatalytic activity, J. Alloy. Compd. 590 (2014) 9–14.
[42] F. Guo, W. Shi, X. Lin, G. Che, Hydrothermal synthesis of graphitic carbon nitride–$BiVO_4$ composites with enhanced visible light photocatalytic activities and the mechanism study, J. Phys. Chem. Solids 75 (2014) 1217–1222.
[43] C. Li, S. Wang, T. Wang, Y. Wei, P. Zhang, J. Gong, Monoclinic porous $BiVO_4$ networks decorated by discrete g-C_3N_4 nano-islands with tunable coverage for highly efficient photocatalysis, Small 10 (2014) 2783–2790.
[44] J. Zhang, F. Ren, M. Deng, Y. Wang, Enhanced visible-light photocatalytic activity of a g-C_3N_4/$BiVO_4$ nanocomposite: a first-principles study, Phys. Chem. Chem. Phys. 17 (2015) 10218–10226.
[45] J. Zhao, J. Yan, H. Jia, S. Zhong, X. Zhang, L. Xu, $BiVO_4$/g-C_3N_4 composite visible-light photocatalyst for effective elimination of aqueous organic pollutants, J. Mol. Catal. A-Chem. 424 (2016) 162–170.
[46] N. Tian, H. Huang, Y. He, Y. Guo, T. Zhang, Y. Zhang, Mediator-free direct Z-scheme photocatalytic system: $biVO_4$/g-C_3N_4 organic-inorganic hybrid photocatalyst with highly efficient visible-light-induced photocatalytic activity, Dalton Trans. 44 (2015) 4297–4307.
[47] L. Jing, Y. Xu, S. Huang, M. Xie, M. He, H. Xu, H. Li, Q. Zhang, Novel magnetic $CoFe_2O_4$/Ag/Ag_3VO_4 composites: highly efficient visible light photocatalytic and antibacterial activity, Appl. Catal. B-Environ. 199 (2016) 11–22.
[48] W. Zhao, Y. Guo, S. Wang, H. He, C. Sun, S. Yang, A novel ternary plasmonic photocatalyst: ultrathin g-C_3N_4 nanosheet hybrided by Ag/$AgVO_3$ nanoribbons with enhanced visible-light photocatalytic performance, Appl. Catal. B-Environ. 165 (2015) 335–343.
[49] H. Lin, J. Cao, B. Luo, B. Xu, S. Chen, Synthesis of novel Z-scheme AgI/Ag/AgBr composite with enhanced visible light photocatalytic activity, Catal. Commun. 21 (2012) 91–95.
[50] J. Fu, S. Cao, J. Yu, Dual Z-scheme charge transfer in TiO2–Ag–Cu_2O composite for enhanced photocatalytic hydrogen generation, J. Materiomics 1 (2015) 124–133.
[51] X. She, H. Xu, Y. Xu, J. Yan, J. Xia, L. Xu, Y. Song, Y. Jiang, Q. Zhang, H. Li, Exfoliated graphene-like carbon nitride in organic solvents: enhanced photocatalytic activity and highly selective and sensitive sensor for the detection of trace amounts of Cu^{2+}, J. Mater. Chem. A 2 (2014) 2563.
[52] Z.H. Ai, W.K. Ho, S.C. Lee, L.Z. Zhang, Efficient photocatalytic removal of NO in indoor air with hierarchical bismuth oxybromide nanoplate microspheres under visible light, Environ. Sci. Technol. 43 (2009) 4143–4150.
[53] D. Dimitrakopoulou, I. Rethemiotaki, Z. Frontistis, N.P. Xekoukoulotakis, D. Venieri, D. Mantzavinos, Degradation, mineralization and antibiotic inactivation of amoxicillin by UV-A/TiO_2 photocatalysis, J. Environ. Manage. 98 (2012) 168–174.
[54] Y. Chen, K. Liu, Preparation and characterization of nitrogen-doped TiO_2/diatomite integrated photocatalytic pellet for the adsorption-degradation of tetracycline hydrochloride using visible light, Chem. Eng. J. 302 (2016) 682–696.
[55] Y. Chao, W. Zhu, F. Chen, P. Wang, Z. Da, X. Wu, H. Ji, S. Yan, H. Li, Commercial diatomite for adsorption of tetracycline antibiotic from aqueous solution, Sep. Sci. Technol. 49 (2014) 2221–2227.
[56] R.R. Sharma, S. Chellam, Temperature and concentration effects on electrolyte transport across porous thin-film composite nanofiltration membranes: pore transport mechanisms and energetics of permeation, J. Colloid. Interface Sci. 298 (2006) 327–340.
[57] H. Xiao, R. Liu, X. Zhao, J. Qu, Enhanced degradation of 2,4-dinitrotoluene by ozonation in the presence of manganese(II) and oxalic acid, J. Mol. Catal. A-Chem. 286 (2008) 149–155.
[58] S. Wang, D. Li, C. Sun, S. Yang, Y. Guan, H. He, Synthesis and characterization of g-C_3N_4/Ag_3VO_4 composites with significantly enhanced visible-light photocatalytic activity for triphenylmethane dye degradation, Appl. Catal. B-Environ. 144 (2014) 885–892.
[59] J. Yang, D. >He, Synthesis and characterization of g-C_3N_4/Ag_3VO_4 composites with significantly enhanced visible-light photocatalytic activity for triphenylmethane dye degradation, Appl. Catal. B-Environ. 144 (2014) 885–892.
[59] J. Yang, D. Chen, Y. Zhu, Y. Zhang, Y. Zhu, 3D-3D porous Bi_2WO_6/graphene hydrogel composite with excellent synergistic effect of adsorption-enrichment and photocatalytic degradation, Appl. Catal. B-Environ. 205 (2017) 228–237.